

1 **Interannual variability of air-sea exchange of mercury in the**  
2 **global ocean: the “seesaw effect” in the equatorial Pacific**  
3 **and contributions to the atmosphere**

4 Shaojian Huang<sup>1</sup> and Yanxu Zhang<sup>1\*</sup>

5 <sup>1</sup>School of Atmospheric Sciences, Nanjing University, Nanjing 210023, China

6 \*Correspondence to: Yanxu Zhang ([zhangyx@nju.edu.cn](mailto:zhangyx@nju.edu.cn))

7

8 **Key Points:**

- 9 • We spot a latitudinal pattern with a smaller variability in the mid-latitudes  
10 (6.4%-8.5%) and a large one in the Arctic and Equator (15%).
- 11 • A seesaw pattern in equatorial Pacific is found for evasion flux anomaly  
12 ( $\pm 10\%$ -20%) between El Niño and La Niña events.
- 13 • A higher atmospheric Hg (1-2%) in northern hemisphere is simulated due to  
14 higher ocean evasion, consistent with the observations (1-11%).

15

16

17

18

19

20

21

22

23

24

## 25 Abstract

26 Air-sea exchange of mercury (Hg) is influenced by meteorological factors that have  
27 substantial interannual variability. Here we investigate its interannual variability and  
28 influencing factors by using the MITgcm ocean model. We elucidate a latitudinal pattern  
29 with a relatively small variability in the mid-latitudes (6.4%-8.5%) and a large one in  
30 the Arctic and Equator (15%). Wind speed, salinity, and sea ice dominate the patterns in  
31 equatorial, mid-, and high-latitude oceans, respectively. A *seesaw pattern* in  
32 equatorial Pacific is found between El Niño and La Niña events, owing to wind speed  
33 anomaly caused by the variation of Walker circulation. A higher atmospheric Hg  
34 concentration (1-2%) in northern hemisphere is found by the GEOS-Chem simulation  
35 due to higher ocean evasion fluxes, consistent with the CAMNet and EMEP (1-11%)  
36 observations. Besides, a slight fluctuation in the upper tropospheric ( $\pm 0.5\%$ ) reveals a  
37 potential contribution from the ocean evasion for interannual variability of  
38 tropospheric Hg.

## 39 Plain Language Summary

40 Mercury is the only metal that is a liquid at room temperature. The strong volatility  
41 makes mercury behave like a noble gas in the atmosphere. Like other gases such as  
42 CO<sub>2</sub>, mercury has an active air-sea exchange, which has an important implication to  
43 the biogeochemical cycle of this toxic element. While it is known that the air-sea  
44 exchange is the largest term in the global biogeochemical cycle of mercury, the  
45 interannual variability and controlling factors remain elusive. We employ a  
46 state-of-the-art three-dimensional ocean model to investigate this issue in this study.  
47 We find a latitudinal pattern with a relatively small variability in the mid-latitudes and a  
48 large one in the Arctic and Equator. A “seesaw pattern” is found in equatorial Pacific  
49 between El Niño and La Niña events, owing to the wind speed anomaly caused by the  
50 oscillating warming and cooling pattern. Meanwhile, a variability of atmospheric  
51 concentration in the northern hemisphere is associated with this pattern. Within the  
52 context of climate change and anthropogenic emission controls proposed by the  
53 Minamata Convention for Mercury, our work helps to distinguish the natural  
54 variability and trend of mercury levels in the environment.

## 55 1 Introduction

56 Mercury (Hg) is a toxic element that is ubiquitous in the environment (Outridge et al.,  
57 2018). It comes from both natural (e.g. volcanic eruption) and anthropogenic sources  
58 (e.g. fossil fuel combustion, metal mining, and smelting) (Horowitz et al., 2014). Two  
59 major chemical forms of Hg exist in the environment: elemental form (Hg<sup>0</sup>) that has  
60 an atmospheric lifetime of 0.5-1 year and undergoes long-range transport; and  
61 divalent form (Hg<sup>II</sup>) that has a shorter atmospheric lifetime (~1 week) and is deposited  
62 near source regions (Selin et al., 2007). Before being buried in deep-sea sediment at  
63 the millennium time scale, Hg can be transported and recycled among the global  
64 atmosphere, land, and oceans (Outridge et al., 2018). Here, we focus on the air-sea

65 exchange of  $\text{Hg}^0$ , which is the largest exchange term between different environmental  
66 compartments in global Hg cycle (Horowitz et al., 2017).

67 The air-sea exchange of  $\text{Hg}^0$  is a bidirectional diffusion process that is driven by the  
68 concentration gradients across the atmospheric and seawater interface (Soerensen et  
69 al., 2013). The direction of exchange is mainly upward (i.e. evasion from the ocean to  
70 the atmosphere) as the  $\text{Hg}^0$  in the surface ocean is often supersaturated (Andersson et  
71 al., 2008; Mason et al., 2001). The magnitude of  $\text{Hg}^0$  exchange flux is influenced by  
72 temperature, wave condition, biological film, and turbulence in the atmosphere and  
73 ocean surface microlayers, and is typically parameterized as a function of wind speed  
74 (Esters et al., 2017). In the marine boundary layer, meteorological conditions such as  
75 temperature and wind speed present significantly interannual variability, which is often  
76 associated with teleconnections and oscillations of the climate system (Grimm &  
77 Natori, 2006; Romero-Centeno et al., 2003). One example is the El Niño-Southern  
78 Oscillation (ENSO), characterized as the anomaly in sea surface temperature (SST)  
79 through the eastern equatorial Pacific Ocean (Guilderson & Schrag, 1998). The shift of  
80 SST would cause the anomalies in sea level pressure and convection, which account for  
81 the seasonal and interannual variability of surface wind and rainfall over this region  
82 (Janowiak & Arkin, 1991; Wang & Enfield, 2001). In this study, we will examine if the  
83 variabilities in meteorological conditions would result in the interannual variability of  
84  $\text{Hg}^0$  air-sea exchange fluxes.

85 The variability in ocean evasion can influence the atmospheric level of  $\text{Hg}^0$  as the ocean  
86 accounts for more than one-third of the global total Hg sources for the atmosphere  
87 (Soerensen et al., 2013). Elevated atmospheric  $\text{Hg}^0$  concentrations in an inland site  
88 were observed when a springtime nor'easter carried the outgassing from the ocean  
89 surface (Sigler et al., 2009). Likewise, in coastal stations such as the Mace Head,  
90 Ireland and the Cape Point, South Africa, significant interannual variability of gaseous  
91 Hg were observed (Ebinghaus et al., 2011; Fisher et al., 2013; Slemr et al., 2008).  
92 Slemr et al. (2016) also found an association between the variabilities of Hg  
93 concentration and ENSO. Another objective of this study is thus to examine the  
94 potential contribution of  $\text{Hg}^0$  evasion to the tropospheric  $\text{Hg}^0$  levels.

## 95 **2 Methodology**

### 96 **2.1 MITgcm model**

97 We use the global three-dimensional model MITgcm to stimulate the chemistry and  
98 transport of Hg in the global ocean. Details of this model were described in Zhang et  
99 al (2019). The model has a horizontal resolution of  $1^\circ \times 1^\circ$  and 50 vertical levels. The  
100 resolution is higher over the Arctic ( $40 \text{ km} \times 40 \text{ km}$ ) and the equator ( $\sim 0.5^\circ \times 1^\circ$ ) to  
101 better represent the ocean currents. Advection and diffusion of Hg are calculated  
102 according to the ocean state estimates from the Estimating the Circulation & Climate  
103 of the Ocean (ECCO v4) climatology (Forget et al., 2015). The meteorological data  
104 that serve as the upper boundary layer of the ocean (e.g. wind speed, air temperature,

105 precipitation, short-wave and long-wave radiation) are from the ERA-Interim  
 106 re-analysis fields spanning 1992-2017 (Dee et al., 2011). The air-sea exchange flux of  
 107  $Hg^0$  is calculated as follow (Andersson et al., 2008; Fu et al., 2010; Wanninkhof,  
 108 1992):

$$109 \quad F = K_w(DGM - GEM/H(T)) \quad (1)$$

110 where  $F$  represents the air-sea exchange flux ( $ng\ m^{-2}\ h^{-1}$ );  $K_w$  is the gas exchange  
 111 velocity (aka piston velocity,  $cm\ h^{-1}$ );  $GEM$  represents the gaseous elemental  $Hg^0$  ( $ng$   
 112  $m^{-3}$ ) in the atmosphere; and  $DGM$  is the dissolved gaseous  $Hg^0$  in seawater.  $H(T)$  is  
 113 the dimensionless partitioning coefficient for  $Hg^0$  between the atmosphere and  
 114 seawater. The parametrization of  $K_w$  follows Soerensen et al (2010) and Nightingale et  
 115 al (2000):

$$116 \quad K_w = 0.31u_{10}^2(S_{c_{Hg}}/S_{c_{CO_2}})^{-0.5} \quad (2)$$

117 where  $S_{c_{Hg}}$  and  $S_{c_{CO_2}}$  are Schmidt numbers of  $Hg^0$  and  $CO_2$ , respectively. Henry's law  
 118 coefficient for  $Hg^0$  is from Andersson (2008):

$$119 \quad H(T) = exp(-2403.3/T + 6.92) \quad (3)$$

120 where  $T$  is the seawater temperature.

121 The atmospheric deposition flux of  $Hg^{II}$  and  $Hg^0$  concentrations in the marine  
 122 boundary layer are from the GEOS-Chem model (Zhang et al., 2019). The model is  
 123 run for 1992-2016 with initial conditions from previous model output (Zhang et al.,  
 124 2020) and the first two years are discarded as spin-up time.

## 125 2.2 GEOS-Chem model

126 We use the GEOS-Chem model (version v 12.2.1) (www.geos-chem.org) to simulate  
 127 the impact of  $Hg^0$  evasion flux on the atmospheric levels of Hg. The detail of the  
 128 model is described by Horowitz et al (2017). This model is driven by assimilated  
 129 meteorological data archived from the Goddard Earth Observing System (GEOS) of  
 130 the NASA Global Modeling and Data Assimilation Office (GMAO), with a horizontal  
 131 resolution of  $4^\circ$  latitude by  $5^\circ$  longitude and 47 vertical eta levels. Three atmospheric  
 132 Hg tracers including elemental mercury ( $Hg^0$ ), divalent mercury ( $Hg^{II}$ ), and  
 133 particulate mercury ( $Hg^P$ ) are simulated in this model. The model contains the  
 134 oxidation of  $Hg^0$  by Br atom and the in-cloud reduction of  $Hg^{II}$ . The partitioning  
 135 between  $Hg^{II}$  and  $Hg^P$  is modeled following Amos et al. (2012). The model also  
 136 includes wet deposition of  $Hg^{II}$  and  $Hg^P$  and dry deposition of all three species. The  
 137 model is driven by the anthropogenic emission inventory of Hg developed by Zhang  
 138 et al. (2016). The model also considers natural emissions and re-emissions from soil  
 139 and snow (Selin et al., 2008). The re-emissions of  $Hg^0$  from the ocean are specified as  
 140 a constant model input, which is from the output of the MITgcm model. We use the  
 141 ocean evasion fluxes during different phases of the ENSO cycle, and the differences

142 of the resulted atmospheric  $\text{Hg}^0$  concentrations are calculated. The model is run for  
143 five years for each ocean evasion scenario, and the results of the last three years are  
144 analyzed.

### 145 2.3 Observation datasets

146 Atmospheric Hg concentration data used in this study are from Canadian Atmospheric  
147 Mercury Network (CAMNet), and European Monitoring and Evaluation Program  
148 (EMEP) networks. These observation data are used for verifying the calculated trends  
149 of our simulations.

150 Decreasing trends are spotted for the original time series of annual Hg concentration  
151 in different observation sites (Zhang et al., 2016). We conduct a linear regression for  
152 the atmospheric  $\text{Hg}^0$  (or total gaseous Hg, TGM) concentrations with time as an  
153 independent variable. The calculated slope is tested by a parametric t-test for  
154 significance ( $\alpha=0.05$ ) (Xu et al., 2006). If significant, the decreasing trends are  
155 removed from the time series by adding the product of slope and time increment.

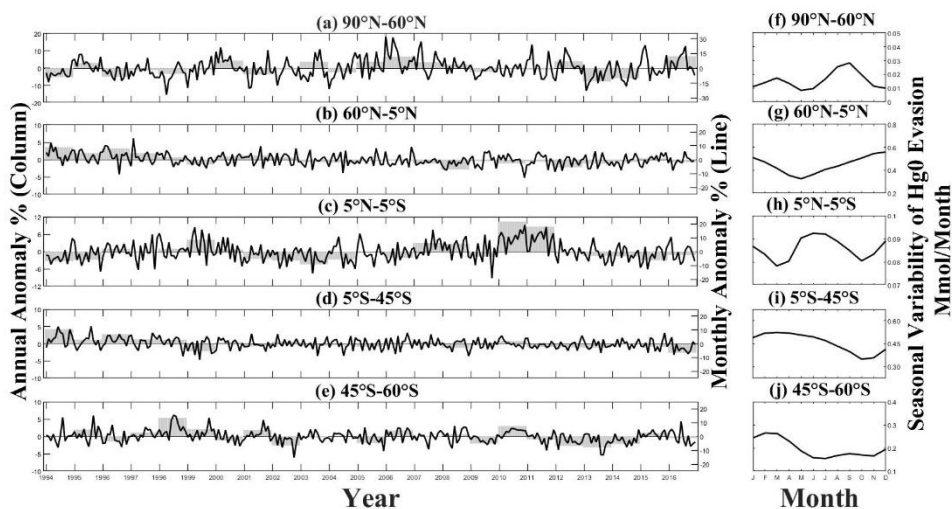
## 156 3 Result and Discussion

### 157 3.1 Variability of $\text{Hg}^0$ evasions

158 Globally, the  $\text{Hg}^0$  evasion flux varies between 18.7-19.4 Mmol/y during 1994-2016. A  
159 distinct latitudinal pattern emerges for the interannual variability of  $\text{Hg}^0$  evasion flux in  
160 the global oceans ([Fig. 1, S1-4](#)). The model indicates that the interannual variability of  
161  $\text{Hg}^0$  evasion is relatively small in the mid-latitudes. The relative ranges [defined as  
162 (maximum-minimum)/mean] of annual evasion flux are 6.4% and 7.0% in the  
163 northern and southern mid-latitude oceans, respectively, and 8.5% for the Southern  
164 Ocean. The interannual variability is high over the Arctic Ocean ( $\pm 10\%$ ), which has  
165 been mentioned by Fisher et al. (2013). However, a more pronounced fluctuation is  
166 simulated for the equatorial regions with a relative range of 15%, with higher  
167 variability for the equatorial Pacific (20%) and Atlantic (22%) Oceans than the  
168 equatorial Indian Ocean (9.6%) ([Fig. S3](#)).

169 Substantial seasonal variability exists for  $\text{Hg}^0$  evasion fluxes as noted by previous  
170 studies (Soerensen et al., 2010; Song et al., 2015; Strode et al., 2007). The highest  $\text{Hg}^0$   
171 evasions are simulated in fall and the lowest in spring in the mid- and high-latitude  
172 oceans in both hemispheres ([Fig. 1 f-g, i-j](#)), reflecting the seasonal cycle of the  
173 precipitation, which influences the amount of atmospheric Hg deposition and  
174 subsequently the size of the available pool for  $\text{Hg}^0$  evasion from the surface ocean.  
175 The seasonal cycle of ocean mixed layer depth also reinforces this pattern.  
176 Entrainment starting in spring brings up Hg-rich waters from the subsurface ocean,  
177 and detrainment in fall decreases the amount of Hg in the mixed layer (Soerensen et al.  
178 2010). In polar regions, the evasion fluxes are the highest in the summertime due to  
179 the highest temperature and least ice coverage. The seasonal variation of evasion in

180 the tropical oceans are more complex with the highest evasion in boreal winter  
 181 resulting from the strongest wind speed and elevated flux in boreal summer due to  
 182 larger precipitation in the intertropical convergence zone (Zhang et al., 2019).



183

184 **Figure 1.** Monthly and annual anomaly (a-e) and monthly mean (f-j) of Hg<sup>0</sup> evasion  
 185 fluxes in the Arctic, northern temperate, equator, southern temperate, and the  
 186 Southern Ocean.

187 **3.2 Influencing Factors**

188 **Table 1** shows the influence of meteorological parameters (including wind speed,  
 189 precipitation, air temperature, sea ice fraction, seawater temperature, and salinity) on  
 190 the annual mean Hg<sup>0</sup> evasion fluxes during 1994-2016. Wind speed is the dominant  
 191 factor in controlling the interannual variability of Hg<sup>0</sup> evasion in equatorial oceans,  
 192 except for equatorial Atlantic. For example, Hg<sup>0</sup> evasion has a positive anomaly in  
 193 2010 (+8.8%) and 2011 (+5.4%), consistent with the positive anomaly of wind speed  
 194 (+8.9% and +5.6%, respectively). Inversely, a negative anomaly of Hg<sup>0</sup> evasion  
 195 (-3.6%) is found in 2015, while the anomaly of wind speed in that year is -6.2% (**Fig.**  
 196 **S5**). The correlation coefficients with wind speed are 0.76, 0.55, and 0.21 in the  
 197 equatorial Pacific, Indian, and Atlantic Oceans, respectively. The correlation between  
 198 annual Hg<sup>0</sup> evasion and precipitation amount is rather weak, even though a significant  
 199 correlation relationship was found on a daily time scale (Zhang et al., 2019). The air  
 200 temperature also has a limited impact on evasion due to the relatively high values as  
 201 well as little relative variability in the equatorial regions.

202 **Table 1.** Correlation between annual Hg<sup>0</sup> evasion fluxes and meteorological  
 203 parameters in different ocean regions.

	Factors	T	Prec.	Wind	SST	S	Sea Ice
	N	0.02	-0.33	-0.29	0.52**	-0.44*	-
Pacific	Eq.	-0.63**	-0.26	0.76**	-0.65**	0.21	-
	S	-0.15	0.10	-0.02	-0.21	-0.07	-

	N	0.03	-0.04	0.17	-0.17	-0.36*	-
Indian	Eq.	0.43*	-0.12	0.59**	0.24	-0.18	-
	S	-0.41*	-0.02	-0.17	-0.43**	-0.23	-
	N	-0.57**	-0.02	-0.26	0.26	0.85**	-
Atlantic	Eq	-0.03	-0.42**	0.21	-0.03	0.06	-
	S	-0.17	0.09	-0.09	-0.30	-0.75**	-
Southern Ocean		0.34	0.11	0.17	-0.19	-0.04	-
Arctic		0.10	0.04	0.01	0.44*	-0.24	-0.61**

204 \*\*represents the significant correlation at the level of 0.01 (bilateral); \*represents the significant correlation  
 205 at the level of 0.05 (bilateral).

206 We find significant correlations between salinity and  $Hg^0$  evasion flux in the  
 207 mid-latitudes except for the southern Pacific and the Indian Ocean, reflecting similar  
 208 influencing factors for water evaporation and  $Hg^0$  evasion. Factors such as higher  
 209 temperatures and stronger wind speed can accelerate the air-sea exchange of both  
 210 water and  $Hg^0$ . This suggests that ocean salinity could serve as an indicator of the  
 211 interannual variability of  $Hg^0$  evasion flux.

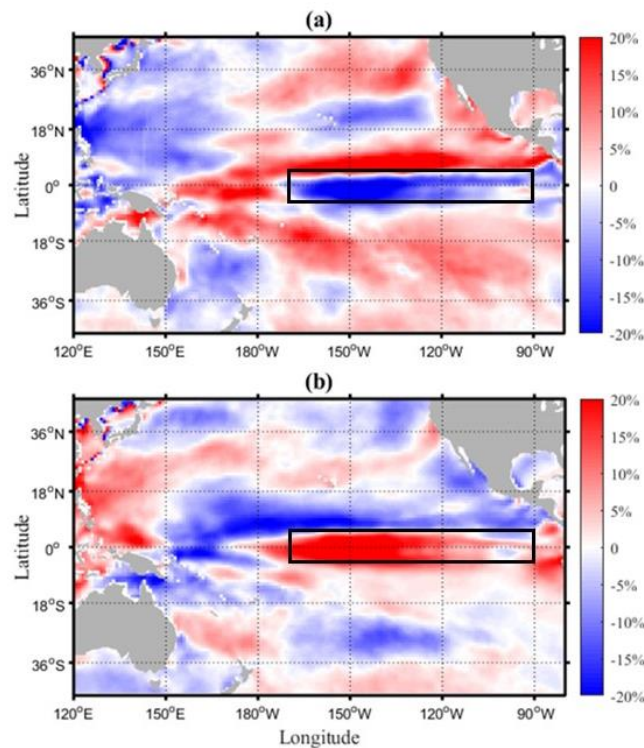
212 In the Arctic Ocean, sea ice is the leading driving factor for the interannual variability  
 213 of  $Hg^0$  evasion (**Fig. S6**). An evident positive anomaly of  $Hg^0$  evasion is spotted in  
 214 2016 (+6.91%) with a negative sea ice anomaly (-3.2%). Indeed, the air-sea exchange  
 215 can be blocked by sea ice thus lower sea ice increases  $Hg^0$  evasion fluxes. Lower sea ice  
 216 also increases the amount of atmospheric  $Hg^{II}$  deposition entering the seawater, which  
 217 would otherwise stay on top of sea ice. Another controlling factor is the SST, which is  
 218 anti-correlated with sea ice cover. The SST peaks in 2016 with a positive anomaly of  
 219 3.2%, which increases the Henry's Law constant for  $Hg^0$  and promotes  $Hg^0$  evasion  
 220 (eq. 3).

### 221 3.3 Seesaw effect of $Hg^0$ evasion in Equatorial Pacific

222 We find the equatorial Pacific Ocean has the largest interannual variability for  $Hg^0$   
 223 evasion fluxes in the global ocean (20%). This could be attributed to the close air-sea  
 224 interactions in this region. Indeed, tremendous heat exchange and SST anomaly occur  
 225 in this region, which can cause anomalies in wind, temperature, and precipitation  
 226 (Vimont et al., 2003; Wallace et al., 1989). Variability of the hydrodynamics between  
 227 eastern and western equatorial Pacific is the essential element in developing the ENSO  
 228 cycle, which could trigger the anomalies of zonal wind stress along the equator  
 229 (Guilderson & Schrag, 1998; Vimont et al., 2003). The expansion and contraction of  
 230 warm water in the warm pool of the Pacific Ocean could also largely affect the  
 231 atmospheric convection (Wang & Enfield, 2001) and contribute to the fluctuation of  
 232  $Hg^0$  evasion. With an average periodicity of 3.8 years (Quinn et al., 1987), ENSO is  
 233 highly likely to influence the interannual variability of  $Hg^0$  evasion in the tropical  
 234 Pacific Ocean.

235 Given that the El-Niño and La Niña events often peak in November, December and  
 236 January (NDJ) (An & Wang, 2001), we contrast the average evasion flux during these  
 237 three months during El Niño (1997, 2004, 2009, and 2015) and La Niña (1996, 1999,

238 2007, and 2010) years ([Fig. 2](#)). The distributions of  $Hg^0$  evasion fluxes for individual  
 239 years are shown in [Fig. S7-8](#)). We find a prominent “seesaw pattern” for the spatial  
 240 distribution of evasion anomaly between El Niño and La Niña years. During El Niño  
 241 years, the evasion flux is 15-20% lower over Equatorial Pacific (5°S-5°N,  
 242 90°W-170°W) and 5-10% higher over western equatorial Pacific (west of 170°W). The  
 243 evasion flux is also 15-20% higher over 5-15°N ([Fig. 2a](#)). The spatial pattern in La  
 244 Niña years is exactly opposite to that in El Niño years with a similar magnitude of  
 245 anomalies ([Fig. 2b](#)). The detailed pattern varies slightly among individual years ([Fig.](#)  
 246 [S7 and S8](#)), but the overall patterns hold.



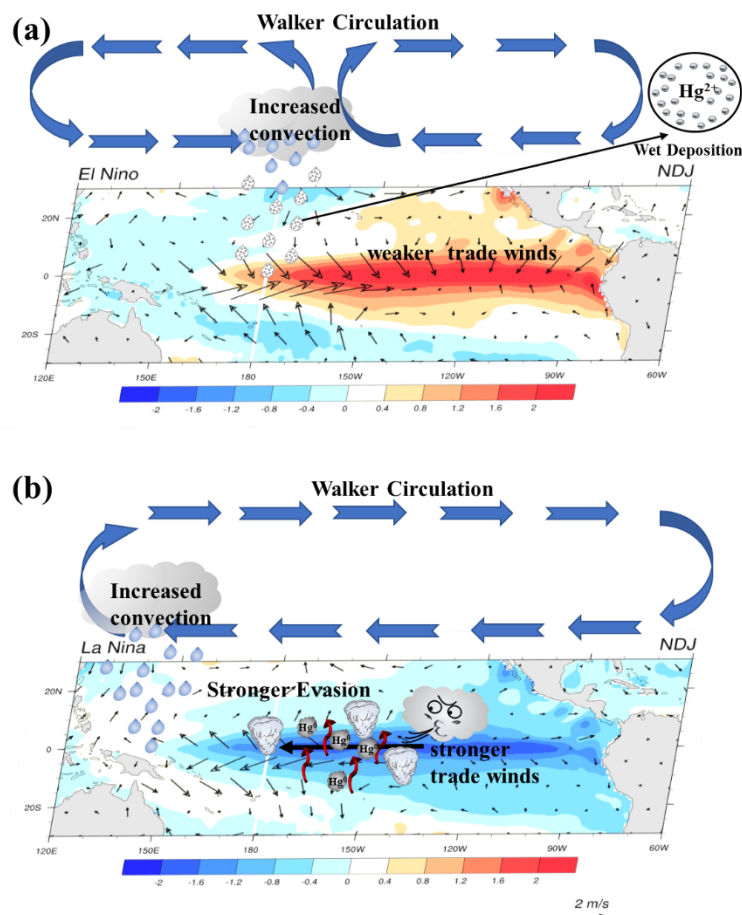
247

248 **Figure 2.**  $Hg^0$  evasion anomaly compared with the average from 1994 to 2016 in  
 249 November-January (NDJ) of tropical Pacific during El Niño and La Niña years. (a)  
 250 The average anomaly of all El Niño events and (b) La Niña events. (Black box  
 251 represents the area within 5°S-5°N, 90°W-170°W)

252 It is known that the “seesaw pattern” marked the interannual variability of SST anomaly  
 253 in eastern and western equatorial Pacific related to ENSO ([Fig. S9](#)). Pronounced  
 254 “seesaw patterns” are also spotted for the wind speed anomaly during the El Niño and  
 255 La Niña event ([Fig. S10](#)). During El Niño years, the wind speed is about 15%-20%  
 256 lower over Equatorial Pacific (120°W to 150°E), while an exactly opposite spatial  
 257 pattern is spotted in La Niña years ([Fig. S10a, b](#)).

258 [Fig. 3](#) illustrates the connection between the anomaly of Walker circulation and  $Hg^0$   
 259 evasion fluxes during El Niño and La Niña events. During the El Niño event, the  
 260 increase of SST in the central-eastern Pacific Ocean decreases the zonal sea surface  
 261 temperature gradient, which causes a collapse of the Walker circulation (Cess et al.,

262 2001). The southeast trades are thus weakened or even reserved, contributing to slower  
 263 air-sea exchange velocity of  $Hg^0$  ( $K_w$ ). Meanwhile, the upward atmospheric motion  
 264 enhances precipitation over the central or eastern Pacific Ocean, which provides more  
 265  $Hg^{II}$  wet deposition to seawater for evasion (Fig. 3a). During the La Niña event, the  
 266 below-average SST across the east-central Equatorial Pacific Ocean enhances the  
 267 Walker circulation, resulting in a strong southeast trade wind and  $Hg^0$  evasion velocity.  
 268 The precipitation is also moved to the western Pacific, causing a positive anomaly of  
 269  $Hg^0$  evasion flux there (Fig. 3b).



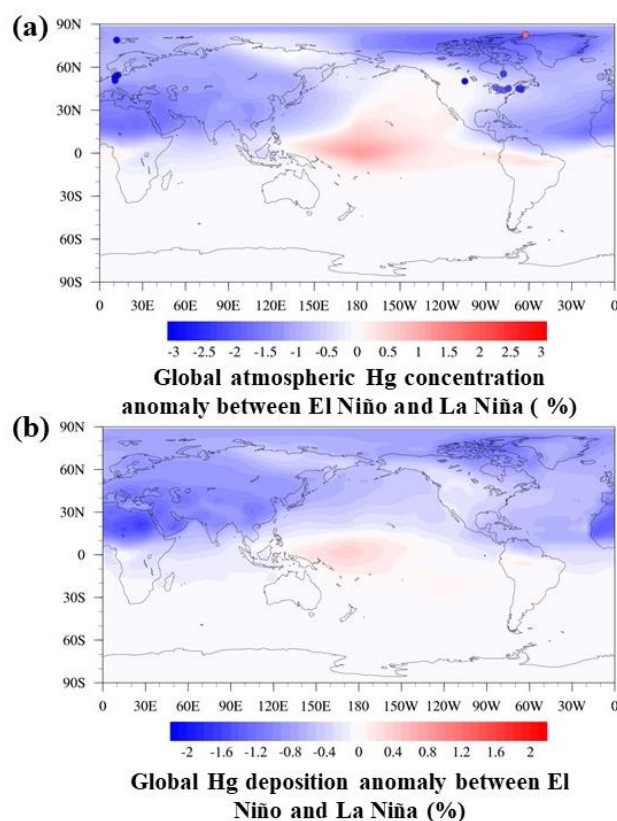
270

271 **Figure 3.** The anomaly of SST and 10 m wind speed in the tropical Pacific Ocean  
 272 during El Niño (a) and La Niña (b) events and its impact on  $Hg^0$  evasion. (Warm color  
 273 represents for a positive anomaly of SST while cold color is for a negative anomaly.  
 274 Arrows present the wind vector).

### 275 3.4 Impact of $Hg^0$ Evasion on Atmospheric Levels

276 **Fig. 4** shows the impact of the variability of  $Hg^0$  evasion on the atmospheric Hg levels  
 277 (their annual anomalies are available in **Fig. S11 -S12**). Compared to the spatial  
 278 pattern of  $Hg^0$  evasion anomaly (Fig. 2), that of the atmospheric Hg level is generally  
 279 smoothed due to the relatively long atmospheric lifetime of  $Hg^0$ . Globally, higher  
 280 concentration (1.5 ppq) and deposition ( $0.06 \text{ ug}\cdot\text{m}^{-2}\cdot\text{a}^{-1}$ ) of Hg levels are modeled

281 during La Niña events comparing to El Niño events. The atmospheric Hg levels are  
 282 reduced in the northern hemisphere during El Niño years as a result of lower evasion  
 283 fluxes (-0.41%), while the differences in the southern hemisphere are relatively small  
 284 (+0.23%). Nevertheless, distinct spatial patterns are modeled for these influences with  
 285 higher Hg levels (10 ppq and  $14 \text{ ug} \cdot \text{m}^{-2} \cdot \text{a}^{-1}$ ) in the equatorial Pacific during El Niño  
 286 events but with higher THg concentration in the Arctic region during La Niña events  
 287 (12 ppq). The average evasion flux in the western equatorial Pacific Ocean ( $5^{\circ}\text{S}$ - $5^{\circ}\text{N}$ ,  
 288  $130^{\circ}\text{E}$ - $170^{\circ}\text{W}$ ) is 6.2 % higher in El Niño events than in La Niña events, which has  
 289 caused the variability of atmospheric concentrations and deposition fluxes in this  
 290 region.



291

292 **Figure 4.** The simulated difference of global a) atmospheric Hg concentrations and b)  
 293 THg deposition during El Niño and La Niña events by the GEOS-Chem model.  
 294 Observed differences in atmospheric Hg concentration in North America (CAMNet)  
 295 and Europe (EMEP) are compared with the simulation and shown as colored dots.  
 296 The modeled higher atmospheric Hg concentrations over the western equatorial  
 297 Pacific Ocean over El Niño years are consistent with measurement data. A previous  
 298 study found short peaks of GEM concentration ( $1.2$ - $2.5 \text{ ng}/\text{m}^3$ ) on the Gunn Point  
 299 Peninsula (northern Australia) during November and December of 2015, a strong El  
 300 Niño event (Howard et al., 2017). While the study attributed the short peaks to  
 301 biomass burnings, the wind directions during these observations indicated that the air  
 302 parcel was mainly from the sea surface (**Fig. S10**). Meanwhile, **Fig. 4a** also displays  
 303 some available surface measurement results from CAMNet and EMEP stations

304 (Details are displayed in **Table S1**). Generally, there is a similar pattern between our  
 305 simulation and observation results in both North America and Europe. In Europe,  
 306 observation sites such as Mace Head and Zeppelin reveal a decreasing trend (-1% to  
 307 -11%) in TGM concentration during El Niño years. Most stations in CAMNet also  
 308 show a lower TGM concentration in El Niño years (-1.8% to -3.1%) comparing to La  
 309 Niña years. This agreement suggests a potential contribution from the variability of  
 310 ocean evasion in these regions, among other factors such as the atmospheric  
 311 circulation, biomass burning, and anthropogenic emissions.

312 The measurements at Alert site present an increasing pattern in El Niño years (+2.2%).  
 313 Based on our simulation, the  $Hg^0$  concentration has a negative anomaly (2 ppq) in the  
 314 Arctic in El Niño events (**Fig. S11b**). It has been found that Arctic sea ice anomaly  
 315 can occur along with ENSO, with less sea ice following by a strong La Niña event  
 316 (Han et al., 2016). The reduced sea ice fraction enhances evasion and subsequently  
 317 atmospheric TGM concentrations during La Niña events in the Arctic (**Table S1**).

318 Besides, overall lower Hg deposition fluxes are modeled over north hemispheric  
 319 terrestrial environment during El Niño years, especially over East Asia ( $12.8$   
 320  $ug \cdot m^{-2} \cdot a^{-1}$ ), South Asia ( $7.65$   $ug \cdot m^{-2} \cdot a^{-1}$ ), West Europe ( $9.23$   $ug \cdot m^{-2} \cdot a^{-1}$ ), and Central  
 321 America ( $9.97$   $ug \cdot m^{-2} \cdot a^{-1}$ ), which indicates potential less ecological toxic effects in  
 322 these regions. Available measurement also shows lower deposition fluxes of Hg in the  
 323 southern Mexico coast in 2004 (an El Niño event) than in 2003 and 2005 (Hansen &  
 324 Gay, 2013).

325 Slemr et al. (2016) have also found an interannual variability of tropospheric (10-12  
 326 km) Hg concentrations, with a time lag of  $8 \pm 2$  months after El Niño. They also  
 327 accounted for this variability to biomass burning because of the large uncertainties of  
 328 estimated Hg emissions from this source. Based on our study, Hg evasion anomaly  
 329 from sea surface during ENSO is also able to fluctuate the global upper tropospheric  
 330 Hg concentrations between El Niño and La Niña years in the northern hemisphere,  
 331 although the trend is relatively weak ( $\pm 0.5\%$ , **Fig. S13**). Therefore, the Hg evasion  
 332 anomaly should be a potential contributor to the interannual variability of tropospheric  
 333 Hg.

334

## 335 **Acknowledgments**

336 The authors gratefully acknowledge financial support from National Natural Science  
 337 Foundation of China (NNSFC) 41875148, Start-up fund of the Thousand Youth Talents  
 338 Plan, Jiangsu Innovative and Entrepreneurial Talents Plan, and the Collaborative  
 339 Innovation Center of Climate Change, Jiangsu Province. Meteorological data used in  
 340 the manuscript are available at

341 <https://apps.ecmwf.int/datasets/data/interim-full-daily/levtype=sfc/>. Atmospheric  
 342 Hg concentration data are available from CAMNet (<http://donnees.ec.gc.ca/data/>),

343 and EMEP (<https://www.emep.int/>) networks.

344

345

## 346 Reference

347 An, S. I., & Wang, B. (2001). Mechanisms of locking of the El Niño and La Niña  
 348 mature phases to boreal winter. *Journal of Climate*, *14*(9), 2164–2176.  
 349 [https://doi.org/10.1175/1520-0442\(2001\)014<2164:MOLOTE>2.0.CO;2](https://doi.org/10.1175/1520-0442(2001)014<2164:MOLOTE>2.0.CO;2)

350 Andersson, M E, Sommar, J., Gårdfeldt, K., & Lindqvist, O. (2008). Enhanced  
 351 concentrations of dissolved gaseous mercury in the surface waters of the Arctic  
 352 Ocean. *Marine Chemistry*, *110*(3), 190–194.  
 353 <https://doi.org/https://doi.org/10.1016/j.marchem.2008.04.002>

354 Andersson, Maria E., Gårdfeldt, K., Wängberg, I., & Strömberg, D. (2008).  
 355 Determination of Henry’s law constant for elemental mercury. *Chemosphere*,  
 356 *73*(4), 587–592. <https://doi.org/10.1016/j.chemosphere.2008.05.067>

357 Cess, R. D., Zhang, M., Wang, P. H., & Wielicki, B. A. (2001). Cloud structure  
 358 anomalies over the tropical Pacific during the 1997/98 El Niño. *Geophysical*  
 359 *Research Letters*, *28*(24), 4547–4550. <https://doi.org/10.1029/2001GL013750>

360 Dee, D. P., Uppala, S. M., Simmons, A. J., Berrisford, P., Poli, P., Kobayashi, S., et al.  
 361 (2011). The ERA-Interim reanalysis: Configuration and performance of the data  
 362 assimilation system. *Quarterly Journal of the Royal Meteorological Society*,  
 363 *137*(656), 553–597. <https://doi.org/10.1002/qj.828>

364 Ebinghaus, R., Jennings, S. G., Kock, H. H., Derwent, R. G., Manning, A. J., & Spain,  
 365 T. G. (2011). Decreasing trends in total gaseous mercury observations in baseline  
 366 air at Mace Head, Ireland from 1996 to 2009. *Atmospheric Environment*, *45*(20),  
 367 3475–3480. <https://doi.org/10.1016/j.atmosenv.2011.01.033>

368 Esters, L., Landwehr, S., Sutherland, G., Bell, T. G., Christensen, K. H., Saltzman, E. S.,  
 369 et al. (2017). Parameterizing air-sea gas transfer velocity with dissipation. *Journal*  
 370 *of Geophysical Research: Oceans*, *122*(4), 3041–3056.  
 371 <https://doi.org/10.1002/2016JC012088>

372 Fisher, J. A., Jacob, D. J., Soerensen, A. L., Amos, H. M., Corbitt, E. S., Streets, D. G.,  
 373 et al. (2013). Factors driving mercury variability in the Arctic atmosphere and  
 374 ocean over the past 30 years. *Global Biogeochemical Cycles*, *27*(4), 1226–1235.  
 375 <https://doi.org/10.1002/2013GB004689>

376 Forget, G., Campin, J.-M., Heimbach, P., Hill, C. N., Ponte, R. M., & Wunsch, C.  
 377 (2015). ECCO version 4: an integrated framework for non-linear inverse modeling  
 378 and global ocean state estimation. *Geosci. Model Dev.*, *8*(10), 3071–3104.

- 379 <https://doi.org/10.5194/gmd-8-3071-2015>
- 380 Fu, X., Feng, X., Zhang, G., Xu, W., Li, X., Yao, H., et al. (2010). Mercury in the  
 381 marine boundary layer and seawater of the South China Sea: Concentrations,  
 382 sea/air flux, and implication for land outflow. *Journal of Geophysical Research*  
 383 *Atmospheres*, *115*(6), 1–11. <https://doi.org/10.1029/2009JD012958>
- 384 Grimm, A. M., & Natori, A. A. (2006). Climate change and interannual variability of  
 385 precipitation in South America. *Geophysical Research Letters*, *33*(19), 1–5.  
 386 <https://doi.org/10.1029/2006GL026821>
- 387 Guilderson, T. P., & Schrag, D. P. (1998). Abrupt shift in subsurface temperatures in  
 388 the tropical Pacific associated with changes in El Niño. *Science*, *281*(5374), 240–  
 389 243. <https://doi.org/10.1126/science.281.5374.240>
- 390 Han, Z., Li, S., Liu, J., Gao, Y., & Zhao, P. (2016). Linear Additive Impacts of Arctic  
 391 Sea Ice Reduction and La Niña on the Northern Hemisphere Winter Climate.  
 392 *Journal of Climate*, *29*(15), 5513–5532.  
 393 <https://doi.org/10.1175/JCLI-D-15-0416.1>
- 394 Hansen, A. M., & Gay, D. A. (2013). Observations of mercury wet deposition in  
 395 Mexico. *Environmental Science and Pollution Research*, *20*(12), 8316–8325.  
 396 <https://doi.org/10.1007/s11356-013-2012-3>
- 397 Horowitz, H. M., Jacob, D. J., Amos, H. M., Streets, D. G., & Sunderland, E. M. (2014).  
 398 Historical Mercury Releases from Commercial Products: Global Environmental  
 399 Implications. *Environmental Science & Technology*, *48*(17), 10242–10250.  
 400 <https://doi.org/10.1021/es501337j>
- 401 Horowitz, H. M., Jacob, D. J., Zhang, Y., Dibble, T. S., Slemr, F., Amos, H. M., et al.  
 402 (2017). A new mechanism for atmospheric mercury redox chemistry: implications  
 403 for the global mercury budget. *Atmospheric Chemistry and Physics*, *17*(10).  
 404 <https://doi.org/10.5194/acp-17-6353-2017>
- 405 Howard, D., Nelson, P. F., Edwards, G. C., Morrison, A. L., Fisher, J. A., Ward, J., et al.  
 406 (2017). Atmospheric mercury in the Southern Hemisphere tropics: Seasonal and  
 407 diurnal variations and influence of inter-hemispheric transport. *Atmospheric*  
 408 *Chemistry and Physics*, *17*(18), 11623–11636.  
 409 <https://doi.org/10.5194/acp-17-11623-2017>
- 410 Janowiak, J. E., & Arkin, P. A. (1991). Rainfall variations in the tropics during  
 411 1986–1989, as estimated from observations of cloud-top temperature. *Journal of*  
 412 *Geophysical Research*, *96*(D Suppl.), 3359–3373.  
 413 <https://doi.org/10.1029/90jd01856>
- 414 Mason, R. P., Lawson, N. M., & Sheu, G.-R. (2001). Mercury in the Atlantic Ocean:  
 415 factors controlling air–sea exchange of mercury and its distribution in the upper

- 416 waters. *Deep Sea Research Part II: Topical Studies in Oceanography*, 48(13),  
 417 2829–2853. [https://doi.org/10.1016/S0967-0645\(01\)00020-0](https://doi.org/10.1016/S0967-0645(01)00020-0)
- 418 Nightingale, P. D., Malin, G., Law, C. S., Watson, A. J., Liss, P. S., Liddicoat, M. I., et  
 419 al. (2000). In situ evaluation of air-sea gas exchange parameterizations using  
 420 novel conservative and volatile tracers. *Global Biogeochemical Cycles*, 14(1),  
 421 373–387. <https://doi.org/10.1029/1999GB900091>
- 422 Outridge, P. M., Mason, R. P., Wang, F., Guerrero, S., & Heimbürger-Boavida, L. E.  
 423 (2018). Updated Global and Oceanic Mercury Budgets for the United Nations  
 424 Global Mercury Assessment 2018. *Environmental Science & Technology*, 52(20),  
 425 11466–11477. <https://doi.org/10.1021/acs.est.8b01246>
- 426 Quinn, W. H., Neal, V. T., & Antunez De Mayolo, S. E. (1987). El Niño occurrences  
 427 over the past four and a half centuries. *Journal of Geophysical Research: Oceans*,  
 428 92(C13), 14449–14461. <https://doi.org/10.1029/JC092iC13p14449>
- 429 Romero-Centeno, R., Zavala-Hidalgo, J., Gallegos, A., & O’Brien, J. J. (2003). Isthmus  
 430 of Tehuantepec wind climatology and ENSO signal. *Journal of Climate*, 16(15),  
 431 2628–2639.  
 432 [https://doi.org/10.1175/1520-0442\(2003\)016<2628:IOTWCA>2.0.CO;2](https://doi.org/10.1175/1520-0442(2003)016<2628:IOTWCA>2.0.CO;2)
- 433 Selin, N. E., Jacob, D. J., Yantosca, R. M., Strode, S., Jaeglé, L., and Sunderland, E. M.  
 434 (2008). Global 3-D land-ocean-atmosphere model for mercury: Present-day  
 435 versus preindustrial cycles and anthropogenic enrichment factors for deposition,  
 436 *Global Biogeochem. Cycles*, 22, GB2011, doi:10.1029/2007GB003040.
- 437 Selin, N. E., Jacob, D. J., Park, R. J., Yantosca, R. M., Strode, S., Jaeglé, L., and Jaffe,  
 438 D. (2007). Chemical cycling and deposition of atmospheric mercury: Global  
 439 constraints from observations, *J. Geophys. Res.*, 112, D02308,  
 440 doi:10.1029/2006JD007450.
- 441 Sigler, J. M., Mao, H., & Talbot, R. (2009). Gaseous elemental and reactive mercury in  
 442 Southern New Hampshire. *Atmos. Chem. Phys.*, 9(6), 1929–1942.  
 443 <https://doi.org/10.5194/acp-9-1929-2009>
- 444 Slemr, F., Brunke, E. G., Labuschagne, C., & Ebinghaus, R. (2008). Total gaseous  
 445 mercury concentrations at the Cape Point GAW station and their seasonality.  
 446 *Geophysical Research Letters*, 35(11), 1–5.  
 447 <https://doi.org/10.1029/2008GL033741>
- 448 Slemr, Franz, Brenninkmeijer, C. A., Rauthe-Schöch, A., Weigelt, A., Ebinghaus, R.,  
 449 Brunke, E. G., et al. (2016). El Niño-Southern Oscillation influence on  
 450 tropospheric mercury concentrations. *Geophysical Research Letters*, 43(4), 1766–  
 451 1771. <https://doi.org/10.1002/2016GL067949>
- 452 Soerensen, A. L., Sunderland, E. M., Holmes, C. D., Jacob, D. J., Yantosca, R. M.,

- 453 Skov, H., et al. (2010). An improved global model for air-sea exchange of mercury:  
 454 High concentrations over the North Atlantic. *Environmental Science and*  
 455 *Technology*, *44*(22), 8574–8580. <https://doi.org/10.1021/es102032g>
- 456 Soerensen, A. L., Mason, R. P., Balcom, P. H., & Sunderland, E. M. (2013). Drivers of  
 457 surface ocean mercury concentrations and air-sea exchange in the West Atlantic  
 458 Ocean. *Environmental Science and Technology*, *47*(14), 7757–7765.  
 459 <https://doi.org/10.1021/es401354q>
- 460 Song, S., Selin, N. E., Soerensen, A. L., Angot, H., Artz, R., Brooks, S., et al. (2015).  
 461 Top-down constraints on atmospheric mercury emissions and implications for  
 462 global biogeochemical cycling. *Atmos. Chem. Phys.*, *15*(12), 7103–7125.  
 463 <https://doi.org/10.5194/acp-15-7103-2015>
- 464 Strode, S. A., Jaeglé, L., Selin, N. E., Jacob, D. J., Park, R. J., Yantosca, R. M., et al.  
 465 (2007). Air-sea exchange in the global mercury cycle. *Global Biogeochemical*  
 466 *Cycles*, *21*(1), 1–12. <https://doi.org/10.1029/2006GB002766>
- 467 Vimont, D. J., Wallace, J. M., & Battisti, D. S. (2003). The seasonal footprinting  
 468 mechanism in the Pacific: Implications for ENSO. *Journal of Climate*, *16*(16),  
 469 2668–2675.  
 470 [https://doi.org/10.1175/1520-0442\(2003\)016<2668:TSMIT>2.0.CO;2](https://doi.org/10.1175/1520-0442(2003)016<2668:TSMIT>2.0.CO;2)
- 471 Wallace, J. M., Mitchell, T. P., & Deser, C. (1989). The Influence of Sea-Surface  
 472 Temperature on Surface Wind in the Eastern Equatorial Pacific: Seasonal and  
 473 Interannual Variability. *Journal of Climate*, *2*(12), 1492–1499.  
 474 [https://doi.org/10.1175/1520-0442\(1989\)002<1492:TIOSST>2.0.CO;2](https://doi.org/10.1175/1520-0442(1989)002<1492:TIOSST>2.0.CO;2)
- 475 Wang, C., & Enfield, D. B. (2001). The tropical western hemisphere warm pool.  
 476 *Geophysical Research Letters*, *28*(8), 1635–1638.  
 477 <https://doi.org/10.1029/2000GL011763>
- 478 Wanninkhof, R. (1992). Relationship between wind speed and gas exchange over the  
 479 ocean. *Journal of Geophysical Research*, *97*(C5), 7373–7382.  
 480 <https://doi.org/10.1029/92JC00188>
- 481 Xu, C., Gong, L., Jiang, T., Chen, D., & Singh, V. P. (2006). Analysis of spatial  
 482 distribution and temporal trend of reference evapotranspiration and pan  
 483 evaporation in Changjiang (Yangtze River) catchment. *Journal of Hydrology*,  
 484 *327*(1), 81–93. <https://doi.org/10.1016/j.jhydrol.2005.11.029>
- 485 Zhang, Y., Jacob, D. J., Horowitz, H. M., Chen, L., Amos, H. M., Krabbenhoft, D. P., et  
 486 al. (2016). Observed decrease in atmospheric mercury explained by global decline  
 487 in anthropogenic emissions. *Proceedings of the National Academy of Sciences*,  
 488 201516312. <https://doi.org/10.1073/pnas.1516312113>
- 489 Zhang, Y., Horowitz, H., Wang, J., Xie, Z., Kuss, J., & Soerensen, A. L. (2019). A

490 Coupled Global Atmosphere-Ocean Model for Air-Sea Exchange of Mercury:  
491 Insights into Wet Deposition and Atmospheric Redox Chemistry. *Environmental*  
492 *Science and Technology*, 53(9), 5052–5061.  
493 <https://doi.org/10.1021/acs.est.8b06205>

494 Zhang, Y., Soerensen, A. L., Schartup, A. T., & Sunderland, E. M. (2020). A Global  
495 Model for Methylmercury Formation and Uptake at the Base of Marine Food  
496 Webs. *Global Biogeochemical Cycles*, 34(2), e2019GB006348.  
497 <https://doi.org/10.1029/2019GB006348>

498